Analysis of microcracking processes in microconcrete under confined compression utilising synchrotron-based ultra-high speed X-ray phase contrast imaging

P. Forquin, C. Francart, M. Sapay, A. Rack, A. Cohen, D. Levi-Hevroni, M. Arrigoni, B. Lukić

▶ **To cite this version:**

P. Forquin, C. Francart, M. Sapay, A. Rack, A. Cohen, et al.. Analysis of microcracking processes in microconcrete under confined compression utilising synchrotron-based ultra-high speed X-ray phase contrast imaging. International Journal of Impact Engineering, 2025, 198, pp.105167. 10.1016/j.ijimpeng.2024.105167 . hal-04924392

HAL Id: hal-04924392
https://hal.science/hal-04924392v1

Submitted on 31 Jan 2025

HAL is a multi-disciplinary open access archive for the deposit and dissemination of scientific research documents, whether they are published or not. The documents may come from teaching and research institutions in France or abroad, or from public or private research centers.

L'archive ouverte pluridisciplinaire **HAL**, est destinée au dépôt et à la diffusion de documents scientifiques de niveau recherche, publiés ou non, émanant des établissements d'enseignement et de recherche français ou étrangers, des laboratoires publics ou privés.

Analysis of microcracking processes in microconcrete under confined compression utilising synchrotron-based ultra-high speed X-ray phase contrast imaging

P. Forquin[1*], C. Francart[1], M. Sapay[1], A. Rack[2], A. Cohen[3], D. Levi-Hevroni[3], M. Arrigoni[4], B. Lukić[2,5]

[1]Univ. Grenoble Alpes, CNRS, Grenoble INP[**], 3SR, 38000 Grenoble, France

[**]Institute of Engineering Univ. Grenoble Alpes

[2] ESRF – The European Synchrotron, CS40220, 38043 Grenoble Cedex 9, France

[3] Department of Physics, NRCN, P.O. Box 9001, Be'er Sheva 8419001, Israel

[4] ENSTA Bretagne, IRDL UMR 6027 CNRS, Brest, France

[5] Henry Royce Institute, Department of Materials, The University of Manchester, UK

Abstract: In the present study, microconcrete (MC) samples were exposed to dynamic quasi-oedometric compression (QOC) tests and visualised *in-situ* by the means of MHz synchrotron X-ray phase-contrast imaging in the ESRF synchrotron in order to analyse the damage mechanisms governing the mechanical behaviour of concrete under high-strain-rate confined compression. To do so, small cylindrical samples were placed in polymeric confinement cell and dynamically compressed along their axial direction using SHPB (Split-Hopkinson Pressure Bar) set-up available in ID19 beamline in the European Synchrotron Radiation Facility (ESRF). The damage process was visualized with MHz X-ray phase-contrast imaging along with an ultra-high-speed camera operating at a recording frequency approximately 1 Mfps (million frames per second *i.e.*, 880 ns interframe time). The axial stress and strain temporal profiles were obtained from standard Kolsky's (SHPB) data processing. In addition, data of radial stress and strain within the sample were deduced from non-linear analysis of the mechanical behaviour of the polycarbonate confining cell instrumented with a strain gauge. Finally, the onset and growth of microcracking observed from the equatorial zone of large spherical pores is correlated with deviatoric and pressure measurements showing how the pore collapse process develops during the applied mechanical loading.

Keywords: Dynamic testing, Synchrotron radiation, quasi-oedometric compression, X-ray phase-contrast imaging, Ultra-high-speed imaging, Concrete, High strain-rates

1. Introduction

The mechanical response of concrete under high confining pressure and high strain-rates is of major importance in various applications such as the vulnerability of concrete structures subjected to hard impact or contact detonation [Forquin, 2017]. In such loading situations, concrete is subjected to shear deformation and compaction (irreversible diminution of the volume) under confinement pressures ranging from few tens to several hundreds of MPa [Hanchak et al., 1992; Li et al., 2005; Forquin et al., 2008a]. Concrete behaviour in terms of shear strength

* Corresponding author: pascal.forquin@univ-grenoble-alpes.fr

and compaction versus pressure and strain-rate need to be describe through a constitutive model in view of numerically simulating the response of concrete structure under such impact or blast loading [Forquin et al., 2015; Antoniou et al., 2018; Perkins et al., 2023; Jacobsen et al., 2023].

During the last decades, several experimental approaches have been developed and used to characterise the mechanical behaviour of concrete under high pressure. For instance, triaxial tests consists in applying a purely hydrostatic pressure on a cylindrical specimen by means of a fluid followed by an additional axial compression. In the first (hydrostatic) stage the volumetric strain is measured as function of the applied hydrostatic pressure by measuring the shortening of the sample, so the compaction law (hydrostatic pressure versus volumetric strain) can be deduced. In the second stage, the axial stress (in absolute value) exceeds lateral pressure exerted by the confinement fluid that is kept constant so the deviatoric stress that corresponds to the axial stress (in absolute value) on withdrawal of the radial stress can be measured as function of the applied axial displacement:

$$\sigma_{deviatoric} = |\sigma_{axial} - \sigma_{radial}| \quad (1)$$

The hydrostatic pressure defined by averaging the three principle stresses is also deduced:

$$P_{hydrostatic} = -\frac{\sigma_{axial}+2\sigma_{radial}}{3} \quad (2)$$

The maximum deviatoric stress reached during the test provides the so-called deviatoric strength. By considering a series of triaxial tests performed at different lateral pressures, a limit state curve is built from the end-points provided by each test. Finally, a limit state curve of the tested concrete can be obtained under static loading [Gabet et al., 2008] or dynamic loading [Fujikake et al., 2000].

An alternative to triaxial tests is the so-called quasi-oedometric compression (QOC) method [Burlion et al., 2001; Forquin et al., 2007; 2008; 2010]. A cylindrical sample is introduced within a confinement cell that consists in a simple (usually metallic) ring of longer height than the sample length. Next, the sample is axially compressed using two compression plugs by means of a conventional mechanical press (in static) or the SHPB apparatus (in dynamic condition). Gradually during the axial compression, the specimen tends to expand along the radial direction, exerting a non-constant lateral pressure against the confinement cell. In the course of the test, the sample experiences a rise of both axial and radial stresses, which results in the deviatoric stress evolving as function of the applied pressure. In addition, provided the axial and radial strain within the sample are known, the volumetric strain (equation (3)) can be obtained as function the hydrostatic pressure (adopting the compaction law).

$$\bar{\varepsilon}_{volumetric} = (1 + \bar{\varepsilon}_{axial})(1 + \bar{\varepsilon}_{radial})^2 - 1 \quad (3)$$

The QOC testing technique was extensively used to characterise the confined behaviour of concrete under static and dynamic loading. Several works focused on investigating the influence of particles size and shape [Forquin et al., 2008c; Arias et al., 2008] and of the porosity [Forquin et al., 2008a] on the confined behavior of particle-reinforced cement composites, but also to analyze the role plaid by free-water on the quasi-static and dynamic confined responses of microconcrete [Forquin et al., 2008b; Forquin et al., 2010], common concrete and high-performance concrete [Piotrowska and Forquin, 2015] and to study the effect of coarse aggregates strength on the static and dynamic behaviour of concrete under high confinement [Piotrowska et al., 2016].

However, the analysis of damage mechanisms (i.e., inception and propagation of microfractures) at microscale driving the overall confined behaviour of concrete at macroscopic scale still remains elusive. Nevertheless, this information is crucial for establishing in a better understanding of the relationship between concrete composition and microstructure, and concrete behaviour under confined compression with the efficiency of the protective solutions in severe conditions.

Over the last years, experimental approaches combining dynamic testing instrumentation and ultra-high-speed phase-contrast X-ray radiography have been developed on the ID19 beamline at the European Synchrotron Radiation Facility (ESRF) [Rack et al. 2024]. Thanks to high brilliance and considerable flux under hard X-ray radiation, it is possible to obtain real-time X-ray imaging information up to single bunch temporal resolution (*i.e.*, 60 ps) within opaque materials [Olbinado et al., 2017], thus allowing for visualisation of non-repeatable damage processes and full-field deformation of materials subjected to high-strain-rate and shock loading. Some examples include visualization of ductile deformation and failure processes involved in Ti-6Al-4V [Cohen et al., 2019], damage inception and propagation under high-rate compression in geomaterials [Farbaniec et al., 2021, Wang et al. 2024] or composite materials [Pournoori et al. 2023, Sun et al. 2024], as well as real-time visualization of high-rate spall failure in geomaterials [Lukić et al., 2022]. However, to the best of our knowledge, this work presents the first real time observation of confined behaviour of concrete under high strain-rate compression with specific aim at investigating the porosity collapse with ultra-high-speed phase-contrast X-ray imaging.

In the present work, the first results obtained on the dynamic QOC experiments performed at the ID19 beamline of The European Synchrotron Radiation Facility (ESRF) are presented and compared to previous experimental data achieved with a larger testing apparatus. The obtained full field radiography data from i*n-situ* ultra-high-speed X-ray phase-contrast imaging illustrate how inception and propagation of dynamic fracturing develops along the axial compression loading.

2. Materials and Methods

2.1 Material microstructure and mixture proportions

Cylindrical specimens of MC were machined with reduced-scale drilling tools. The maximum grain size and means grain size, respectively about 2 mm and 0.5 mm, makes this MC very attractive to perform experiments with relatively small specimens. A similar MC (D_{max} = 5 mm) was previously studied in the past under dynamic quasi-oedometric compression tests [Forquin et al., 2008b; 2010] considering cylindrical sample 29 mm in diameter and 40 mm in length. In the present study, much smaller samples were tested with a diameter ranging from 5 to 7.5 mm and a length ranging from 5.6 to 8 mm. However, the initial length to diameter ratio was kept slightly higher than 1 as in the previous studies.

Table 1. Microconcrete composition

Sand (kg/m3)	1783
Cement (kg/m3)	400
Water (kg/m3)	200
Water/cement	0.5
Max/mean grain size (mm)	2/0.5

2.2 Dimensions of samples and confinement cell tested in ESRF

The MC samples subjected to synchrotron radiation imaging experiments are cylindrical samples from 5 to 7.49 mm in diameter, with an initial length (h_0^{sample}) ranging from 5.66 mm to 8.11 mm (Table 2). The confinement cells are all made of PC (Poly-Carbonate) polymer. The same outer diameter ($Ø_{outer}^{cell}$) equal to 12.7 mm was set for all cells. Two lengths of confining cells (H^{cell}) were considered: 8 and 10 mm in order to consider the different lengths of MC samples. Moreover, three values of inner diameter ($Ø_{inner}^{cell}$) were considered for PC cell in order to match as well as possible with sample diameter. A single strain gauge was installed on each confining cell in the mid-plane of the cell ($z = 0$) and considering a hoop orientation (i.e. perpendicularly towards the ring axis). The PC cell being supposed to be loaded beyond its elastic limit, each confining cell was used only once.

The field of view, 12.8 mm in width and 8 mm in height, is centred towards the MC sample. Therefore, whereas the whole sample length, diameter and confining length can be observed in the field of view, the full diameter of the confining cell could not be visualised.

Table 2. Dimensions of MC samples and PC confinement rings

Materials	Samples	$Ø_{inner}^{cell}$ (mm)	$Ø_{outer}^{cell}$ (mm)	H^{cell} (mm)	h_0^{sample} (mm)
MC-D5 samples	MC-D5_1	5.24	12.7	8	5.66
	MC-D5_2	5.24	12.7	8	6.07
	MC-D5_3	5.0	12.7	8	5.89
	MC-D5_4	5.0	12.7	8	6.02
	MC-D5_5	5.24	12.7	8	6.06
MC-D7.5 samples	MC-D7.5_1	7.49	12.7	10	8.18
	MC-D7.5_2	7.49	12.7	10	8.11
	MC-D7.5_3	7.49	12.7	10	7.63
	MC-D7.5_4	7.49	12.7	10	7.93

2.3 SHPB apparatus and data processing

In the present work, 12.7 mm diameter SHPB facility available in ID19 beamline was used to perform dynamic QOC tests applied to concrete. The system is described in detail in [Cohen et al., 2019]. The lengths of input and output bars are 1310 mm and 1110 mm, respectively. The striker bar, of same diameter is 250 mm in length. The striker, the input bar and the output bar are all made of the high-strength steel (PH 17-4 H900, yield strength 1200 MPa). When the striker hits the free end of the input bar, a compressive incident wave is generated in the input bar. Once the incident wave (ε_i) reaches the specimen, a transmitted pulse (ε_t) develops in the output bar and a reflected pulse (ε_r) travels downstream in the input bar. The input and output forces and the input and output velocities at the specimen faces are deduced from Kolsky's post-treatment of these waves, thanks to strain gauges glued on the input and the output bars according to the following equations [Kolsky, 1949]:

$$\begin{cases} F_{in}(t) = A_b E_b(\varepsilon_i(t) + \varepsilon_r(t)) \\ F_{out}(t) = A_b E_b\big(\varepsilon_t(t)\big) \end{cases}, \tag{4}$$

$$\begin{cases} V_{in}(t) = -c_b(\varepsilon_i(t) - \varepsilon_r(t)) \\ V_{out}(t) = -c_b\big(\varepsilon_t(t)\big) \end{cases}, \tag{5}$$

where A_b is the area of the input and output bars, E_b corresponds to their Young's modulus and c_b is the speed of a 1D wave propagating in these bars ($c_b = \sqrt{E_b/\rho_b}$), considering ρ_b as the density of the bars. According to measurements of density (ρ_b = 7.817) and wave speed (c_b = 5020 m/s) the following Young's modulus was deduced (E_b = 197 GPa). Finally, the mean axial stress and nominal axial strain in the sample are deduced:

$$\overline{\sigma_{axial}}(t) = \frac{F_{in}(t)+F_{out}(t)}{2A_S}, \quad (6)$$

$$\overline{\varepsilon_{axial}}(t) = \int_0^t \frac{V_{out}(u)-V_{in}(u)}{h_0^{sample}} du, \quad (7)$$

where h_0^{sample} is the sample initial length.

2.4 The principle of the measurement of radial stress and strain within the sample

Whereas the axial stress and strain are deduced based on Kolsky's data processing the measurement of radial stress and strain within the sample is more complicated and was the subject of several publications. As detailed in [Forquin et al., 2007; 2008b; 2010] it consists in considering the data of (at least) one strain gauge glued on the outer surface of the confining cell. Provided that the constitutive behavior of the confining cell is known, two distinct numerical simulation involving only the confining vessel are performed by means a finite element modeling (FEM). A ramp of internal pressure is applied to the inner surface of the ring considering lengths equal to the initial and final heights of the concrete sample. From these calculations the relations: $\sigma_{radial(h_{initial})} = f_{initial}\left(\varepsilon_{\theta\theta}^{(z=0,ext)}\right)$ and $\sigma_{radial(h_{final})} = f_{final}\left(\varepsilon_{\theta\theta}^{(z=0,ext)}\right)$ are deduced, so the radial stress in the sample can be computed knowing the current height of the sample (h_S) according to the following linear interpolation:

$$\bar{\sigma}_{radial} = \left(\frac{h_S-h_f}{h_i-h_f}\right) f_{initial}\left(\varepsilon_{\theta\theta}^{(z=0,ext)}\right) + \left(\frac{h_S-h_i}{h_f-h_i}\right) f_{final}\left(\varepsilon_{\theta\theta}^{(z=0,ext)}\right) \quad (8)$$

In a similar way, the (small) radial strain in the sample was deduced based on the same type of data processing:

$$\bar{\varepsilon}_{radial} = \left(\frac{h_S-h_f}{h_i-h_f}\right) g_{initial}\left(\varepsilon_{\theta\theta}^{(z=0,ext)}\right) + \left(\frac{h_S-h_i}{h_f-h_i}\right) g_{final}\left(\varepsilon_{\theta\theta}^{(z=0,ext)}\right) \quad (9)$$

A sensitivity analysis of the processing method to several experimental parameters was conducted in [Forquin et al., 2007; 2008] by processing the data of a series of numerical simulations of QOC test and by comparing the obtained hydrostatic and deviatoric responses to the expected ones (considered constitutive laws for concrete).

2.5 Development and calibration of the PC confining cell

Prior to in-situ QOC tests, a series of dynamic compression test was performed with cylindrical PC samples and considering the SHPB testing set-up described in subsection (2.3). The tested sample was 10 mm in diameter and 5 mm in length. The true axial stress and axial strain was deduced from the classical data processing as described in Equations (4-7) considering for the growth of sample cross-section during the compression test. The Young's modulus of PC being known, the plastic strain was calculated as the axial strain on withdrawal of the elastic strain. The obtained axial stress - plastic strain curve is reported in Fig. 1 and the parameters of the fitted elastoplastic model are reported in Table 3.

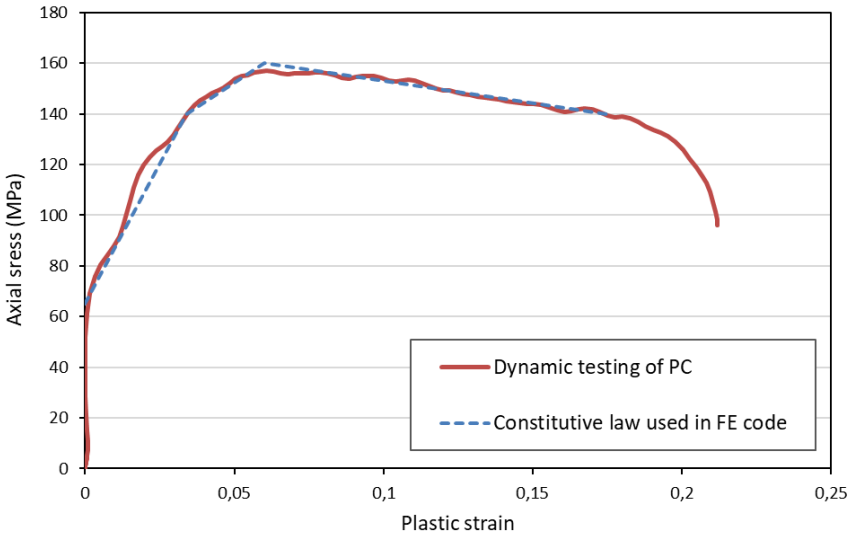

Fig. 1. Mechanical behaviour of PC based on a dynamic compression test performed with SHPB facility in ID19 beamline and identification of the constitutive law (Table 3).

Table 3. Parameters of elastoplastic model used in FE numerical simulation for PC

Young's modulus, Poisson's ratio	5 GPa, 0.42
Plastic strain, Mises stress	0.0, 65 MPa 0.034, 140 MPa 0.06, 160 MPa 0.175, 140 MPa

The constitutive law of PC was introduced in a FE numerical simulation performed with Abaqus FE code. In this calculation, the behavior of a PC ring subjected to an internal pressure is simulated considering an internal pressure continuously increasing from 0 to 100 MPa. Two sets of dimensions were considered for the PC cell. In the first set, the inner diameter ($Ø_{inner}^{cell}$) was fix to 5.14 mm (as an average of MC-D5 sample diameters) and the height of the confining cell (H^{cell}) was fixed to 8 mm. In the second set, the inner diameter ($Ø_{inner}^{cell}$) was fix to 7.49 mm (as the diameter of MC-D7.5 samples) and the height of the confining cell (H^{cell}) was fixed to 10 mm. In both cases the same outer diameter ($Ø_{outer}^{cell}$ = 12.7 mm) was used. In addition, in both cases two heights of applied pressure (h_S) were considered: h_i = 6 mm and h_f = 5.25 mm in case 1 and h_i = 8 mm and h_f = 7 mm in case 2. Finally, in each numerical simulation, the hoop strain was deduced from the radial displacement of the node located on the outer surface of the ring in the symmetry plane (z = 0). The internal pressure versus the outer hoop strain are reported in figure 2. The polynomial equations based on Fig. 2 are reported in Table 4.

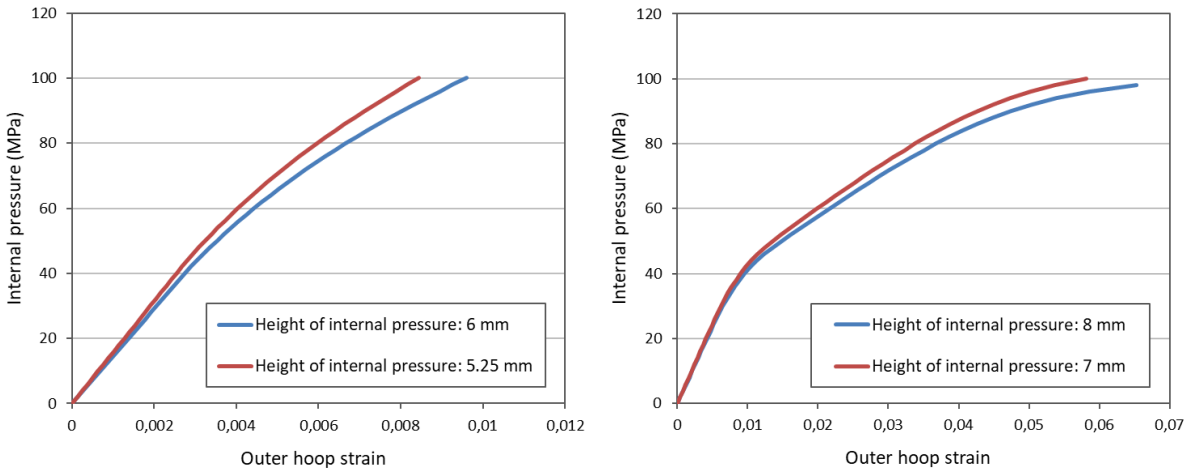

(a) (b)

Fig. 2. Identification of the relation between the measured outer hoop strain and internal pressure applied to a PC ring. (a) Case 1 for MC-D5 samples ($Ø_{inner}^{cell}$ = 5.14 mm, H^{cell} = 8 mm). (b) Case 1 for MC-D7.5 samples ($Ø_{inner}^{cell}$ = 7.49 mm, H^{cell} = 10 mm). In case 1, the height of applied pressure is fixed to h_i = 6 mm and h_f = 5.25 mm. In case 2, the height of applied pressure is fixed to h_i = 8 mm and h_f = 7 mm.

Table 4. Polynomial equations of internal pressure vs outer hoop strain identified from Fig. 2

Case 1		Case 2	
h_i = 6 mm	y = -5,960E+05x^2 + 1,605E+04x	h_i = 8 mm	y = -2,234E+07x^4 + 3,324E+06x^3 - 1,830E+05x^2 + 5,484E+03x
h_f = 5.25 mm	y = -6,538E+05x^2 + 1,734E+04x	h_f = 7 mm	y = -3,128E+07x^4 + 4,210E+06x^3 - 2,105E+05x^2 + 5,853E+03x

2.6 Identification of the deviatoric and hydrostatic behaviour of the MC sample

Finally, the change of deviatoric stress versus the hydrostatic pressure can be deduced based on the Equations (1) and (2) whereas the change of hydrostatic pressure versus volumetric strain can be deduced based on Equations (2) and (3).

3. Results

In the present section, the experimental data obtained from QOC data processing are reported. The deviatoric and hydrostatic response of four MC samples are deduced. Time-resolved observations performed with ultra-high-speed camera are provided.

3.1 Nominal macroscopic stress - strain material response

The experimental data recorded in one MC-D5-1 QOC compression test are reported in Fig. 3. The input signal provided the evolution of incident wave and reflected wave whereas the output signal shows the temporal profile of the transmitted wave. As expected, the amplitude of

transmitted wave is observed to increase (in amplitude) due to the increase of confinement pressure illustrated on the signal of cell strain gauge (black curve).

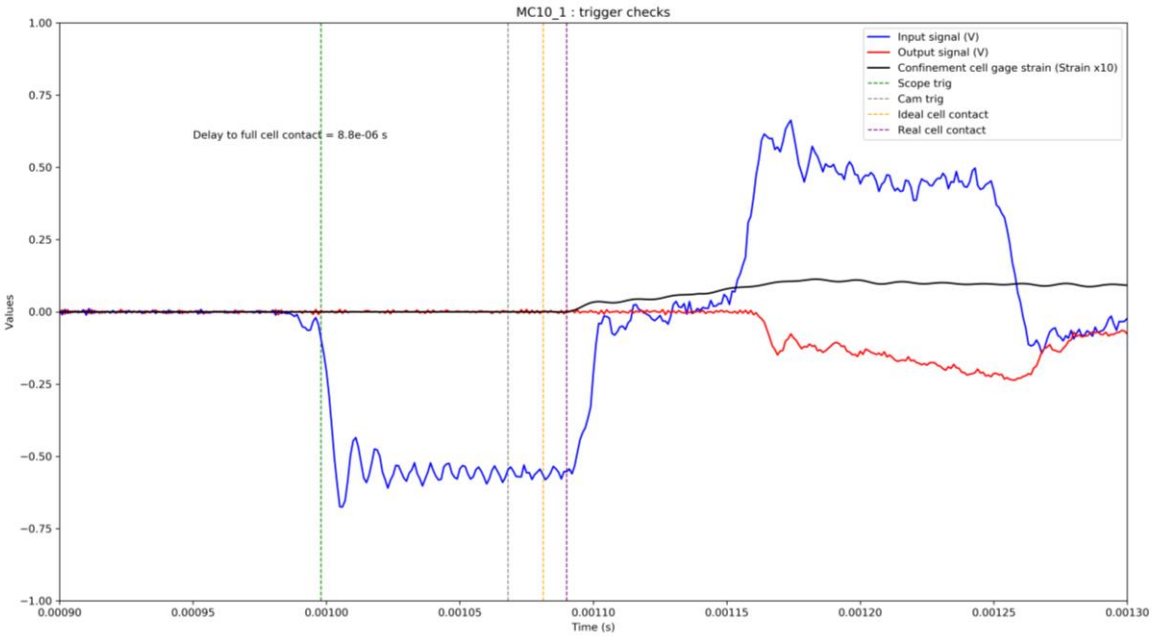

Fig. 3. Experimental data recorded in MC-D5-1 QOC compression test. 'Cam Trig' corresponds to camera triggering. 'Ideal cell contact' corresponds

The processed data of MC-D5-1, 2, 3 and 4 QOC compression tests are reported in Fig. 4. The loading applied to the sample, in terms of nominal axial strain versus time, is almost the same in each test (Fig. 4a). The nominal strain-rate profile shows a level of strain-rate roughly constant (Fig. 4b), as it was expected given the small amplitude of the transmitted wave compared to the incident wave. The maximum level of axial strain (about -12%) is reached thanks to the level of strain-rate maintained during the test (about 1200 s^{-1}) and to the loading time imposed by the round-trip time of wave in the striker (about 100 µs). In the four tests, the outer hoop strain measured by strain gauge has reached about 1% (Fig. 4c), which means that PC cells have greatly exceeded their elastic limit according to Fig. 2. The nominal axial stress (axial force divided by initial sample cross-section) deduced from Kolky's data processing is observed to increase continuously up to 200 MPa (Fig. 4d). Finally, the overall mechanical response of the four tests is quite similar as illustrated in Fig. 4d.

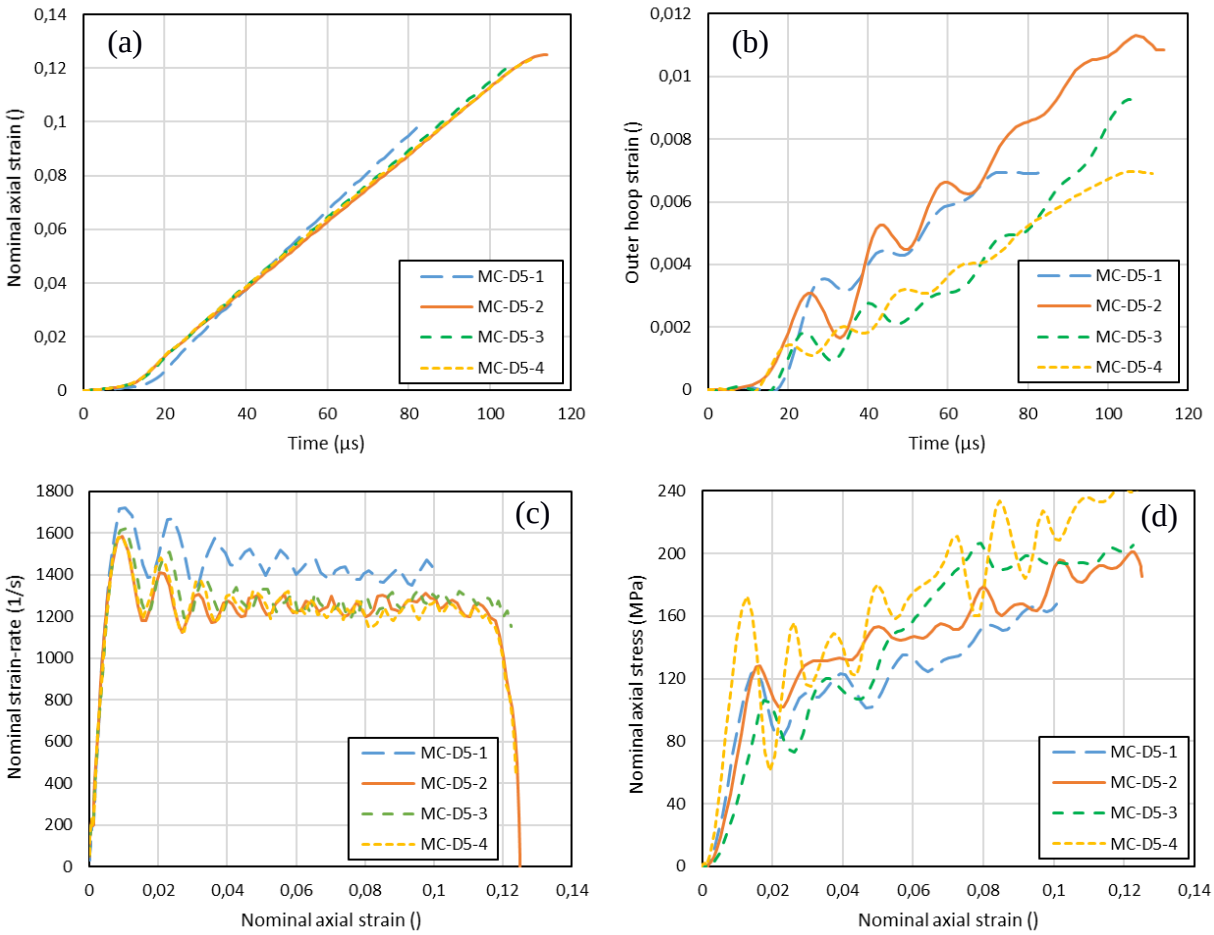

Fig. 4. Processed data from MC-D5-1, 2, 3 and 4 QOC compression tests. (a) Nominal axial strain (absolute value) versus time, (b) Outer hoop strain versus time, (c) Nominal strain-rate and (d) nominal axial stress versus nominal axial strain (absolute value).

3.2 Deviatoric and hydrostatic material response

The temporal profiles of axial stress, radial stress, hydrostatic pressure (Eq. (2)) and deviatoric stress (Eq. (1)) are plotted in Figs. 5a and 5b for MC-D5-1 and MC-D5-2 MC samples. In both tests, the axial stress (in absolute value) quickly rises to 120 MPa and then continues increasing up to 160 MPa (MC-D5-1) and 200 MPa (MC-D5-2). In the meantime, the radial stress within the sample (Eq. (8)) evolves from about 50 MPa and goes up to about 90 MPA (MC-D5-1) and 110 MPa (MC-D5-2). The resulting maximum hydrostatic pressure reaches 120 MPa (MC-D5-1) and 140 MPa (MC-D5-2) for which a deviatoric stress about 80 MPa is noted for both samples. Both tests provide very consistent results. The deviatoric stress versus pressure is plotted for both tests in Fig. 5c. A linear increase of strength is noted in the first regime with a slope close to 1.5. Next, the MC response seems to follow a limit state curve with an almost constant strength of 56 MPa (MC-D5-1) and 75 MPa (MC-D5-2) as calculated by averaging the deviatoric stress over an axial strain from -2% to -10%. By comparing the experimental results with previous results of dynamic QOC tests performed with dry MC [Forquin et al., 2010] it is observed that the increase of strength with pressure observed in the present work is much smaller. The main reason would be the small stiffness of PC confining ring compared to confining ring made of high-strength steel, that contribute to imitate the level of pressure and deviatoric strength reached in the present study. The hydrostratic response (pressure versus volumetric strain) for both tests is plotted in Fig. 5d. Next to the elastic response (grey straight line), a

linear increase of pressure with volumetric strain is observed with a pressure smoothly increaing from 70 MPa to 120 MPa (MC-D5-1) and 140 MPa (MC-D5-2). This response would result from the phenomenon of pore collapse observed subsequently by time-resolved ultra-high speed X-ray imaging.

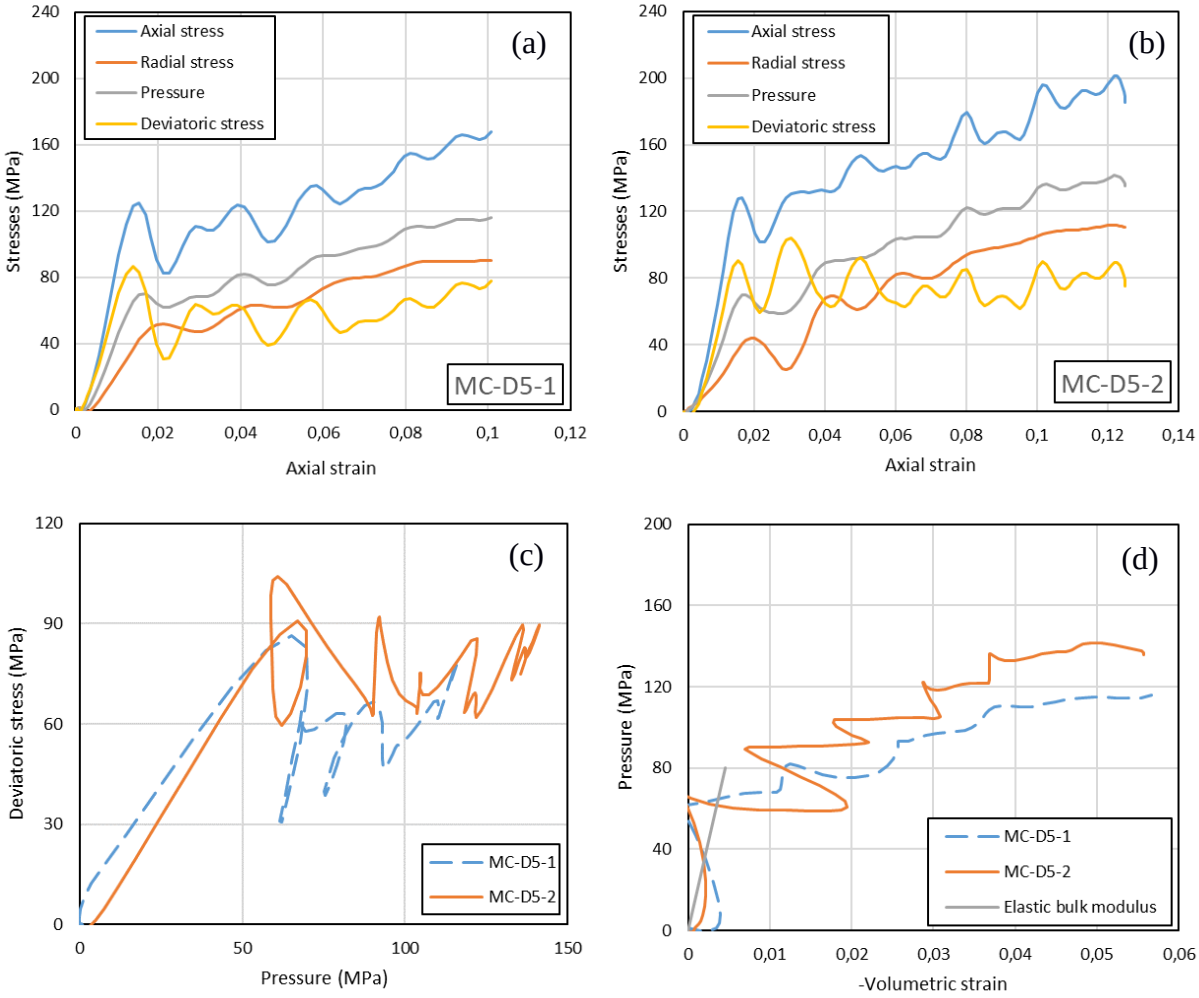

Fig. 5. Processed data from MC-D5-1 and MC-D5-2 QOC compression tests. (a) Stresses versus axial strain (absolute value) in MC-D5-1 test. (b) Stresses versus axial strain (absolute value) in MC-D5-2 test. (c) Deviatoric response (deviatoric stress versus pressure) for both tests. (d) Hydrostatic response (pressure versus volumetric strain) for both tests.

3.3 Time-resolved ultra-high speed X-ray imaging measurements

The sample placed within its PC confinement ring was illuminated by means of polychromatic white X-ray beam emitted by two axially aligned long-period undulators (λ_u=32 mm) with a median radiation energy at 28 keV. The incident beam was conditioned with two in-vacuum slites and filtered with permanent optical windows located along the 145 m long vacuum flight tube for heat moderation, cutting large part of the spectrum within the first harmonics (i.e., bellow 10keV). The beam impinging the sample is of a relatively large field of view (12.8 mm in width and 8 mm in height). The experiments are conducted using the 16-bunch operating mode (i.e., 176 ns bunch separation) having a single bunch pulse integrated over one captured radiograph. The indirect detector assembly consisted of the HPV-X2 ultra-high speed camera (Shimadzu, Japan) lens-coupled to a fast scintillator (LYSO:Ce, Hilger Crystals, UK) and a

folding mirror. The real time visualisation of the cracking process through the thickness of the sample with an interframe time set to 880 ns and exposure time of 200 ns. The sensor has effective 400 × 250 pixel size providing 128 radiographs in burst mode, with a high spatial sampling with respect to the size of the field of view (horizontal and vertical scales: 33.3 pixel/mm). The observation window is centred toward the axis of loading.

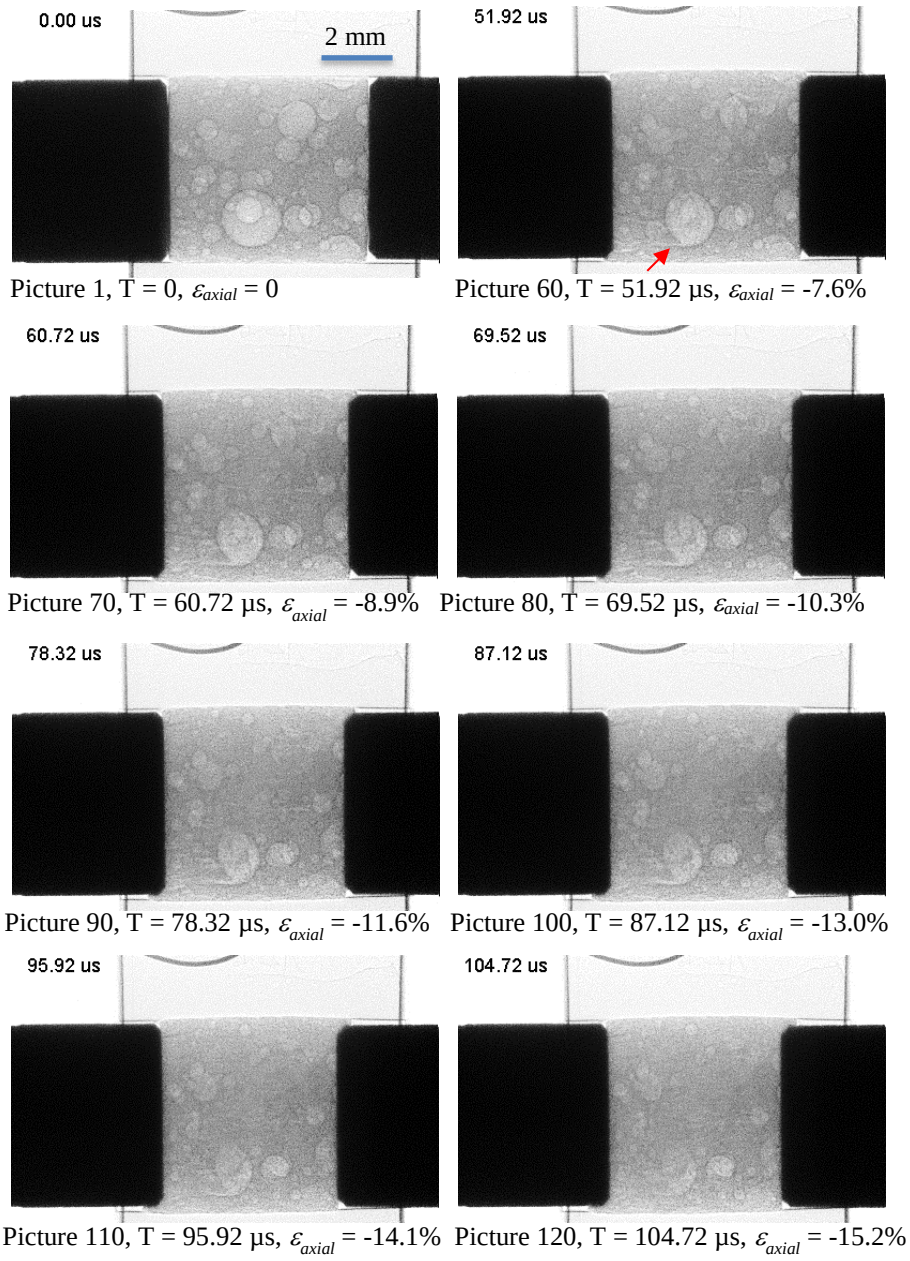

Fig. 6. Time-resolved observations performed with ultra-high-speed camera in MC-D5-1 QOC compression test. Input bar is on the right side. The sample is moving toward the left side. (red arrow: axial crack initiates from the equator of the largest pore and propagated along the axial direction)

The radiographs captured by the ultra-high-speed detector during the MC-D5-1 and MC-D5-2 QOC compression tests are depicted in Figs. 6 and 7. At time T = 0 (prior axial compression) MC-D5-1 sample is observed to be placed in perfect contact with the compression plugs and with the confinement ring. The radiography of the pristine sample indicated a well-defined

contact between the sample and the confinement cell which is verified by the fact that radial stress increases from the beginning of compression loading (Fig. 6). At time T = 69.56 µs the barrelling effect can be observed at the sample-cell contact surface. In addition, a small bead (upper-right corner on the pictures) of material tends to escape from the gap between the plugs and the cell, which illustrates the capability of MC material to deform under confinement loading. It is particularly interesting to observe the deformation of the largest spherical pores (cf. red arrows) in the shape of an ellipse, contrary to smaller pores that seems to keep their spherical shape. It tends to demonstrate that the largest pores seem to crush first. In addition, several cracks oriented along the axial direction can be annoted. In particular the axial crack was clearly initiated from the equator of the largest pore and propagated along the axial direction. In the subsequent radiographs, several pores appear fully crushed whereas the largest pore still remains visible, however having a substantially changed peripheral shape. A possible explanation could be a vault (or arch) effect preventing a whole collapse of this pore.

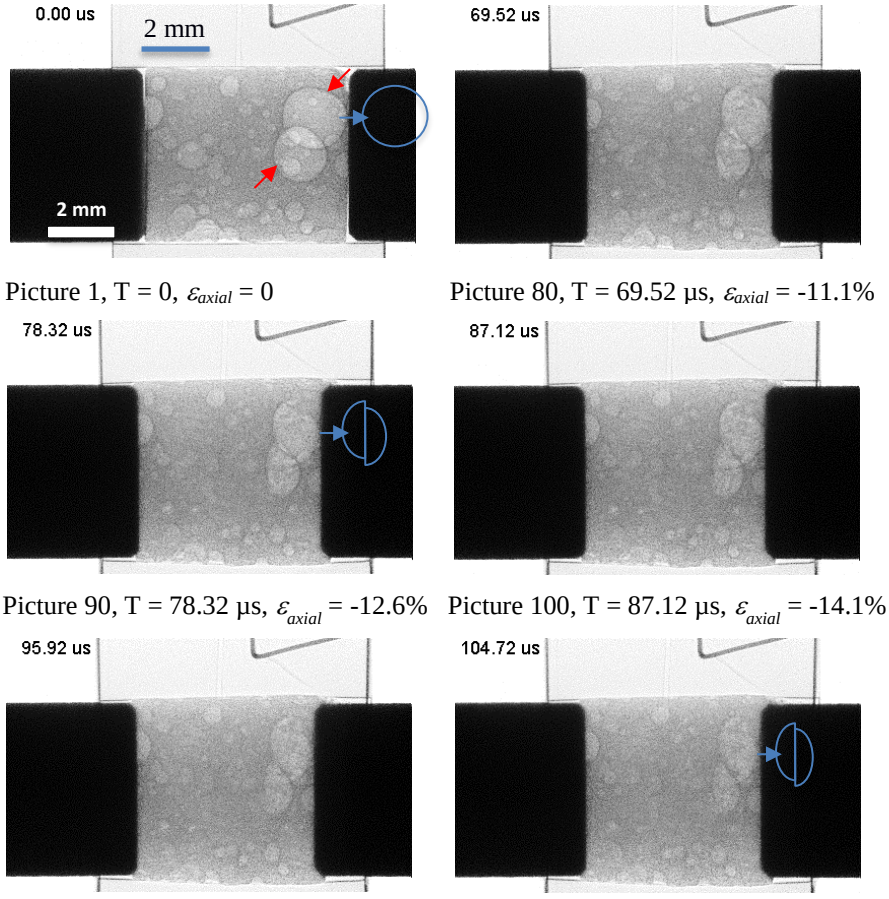

Picture 1, T = 0, ε_{axial} = 0 Picture 80, T = 69.52 µs, ε_{axial} = -11.1%

Picture 90, T = 78.32 µs, ε_{axial} = -12.6% Picture 100, T = 87.12 µs, ε_{axial} = -14.1%

Picture 110, T = 95.92 µs, ε_{axial} = -15.0% Picture 120, T = 104.72 µs, ε_{axial} = -16.2%

Fig. 7. Time-resolved observations performed with ultra-high-speed camera in MC-D5-2 QOC compression test. Input bar is on the right side. The sample is moving toward the left side. (red arrow: large pores, blue circle: shear mode of large pore)

In the case of MC-D5-2 sample, large spherical pores (red arrow, Fig. 7) seem to collapse in a non-symmetric way. Indeed, from picture 80, pore looks like split in two parts and sheared along its mid-plane (see details in Fig. 7). This local deformation phenomenon could be attributed to some initial imperfections at cell-sample interface or at plug-sample interface leading to shearing deformation mode within the sample.

A post-processing of radiographs was carried out to quantify the time-resolved axial strain (Fig. 8) and radial expansion (Fig. 9) of the sample. To do so, the contribution of the phase contrast at the sample-ring material interface was exploited. The radial expansion in MC-D5-1 and MC-D5-2 QOC compression tests was calculated by considering the gradient of grey level at sample border and by averaging the radial displacement (in absolute value) on top and bottom sides. The "radial expansion" is plotted as function of time and axial position in Figs. 9a (MC-D5-1 sample) and 9b (MC-D5-2 sample). As the end of the loading it reaches about 0.2 and 0.25 mm, which corresponds to radial strain from 8 to 10%. Such radial expansion is much stronger than with steel confining cell as reported in [Forquin et al., 2010]. Finally, the radial expansion remains notably homogeneous along the axial position in the case of MC-D5-1 sample due to the good contact between the sample and the confining cell. On the other hand, the radial expansion is more heterogeneous in the case of MC-D5-2 sample. This non-homogenous profile is due to imperfections of the contact quality between the sample and the confinement cell at the beginning of the test but also to the collapse of two pores located near the interface on bottom of pictures in Fig. 7.

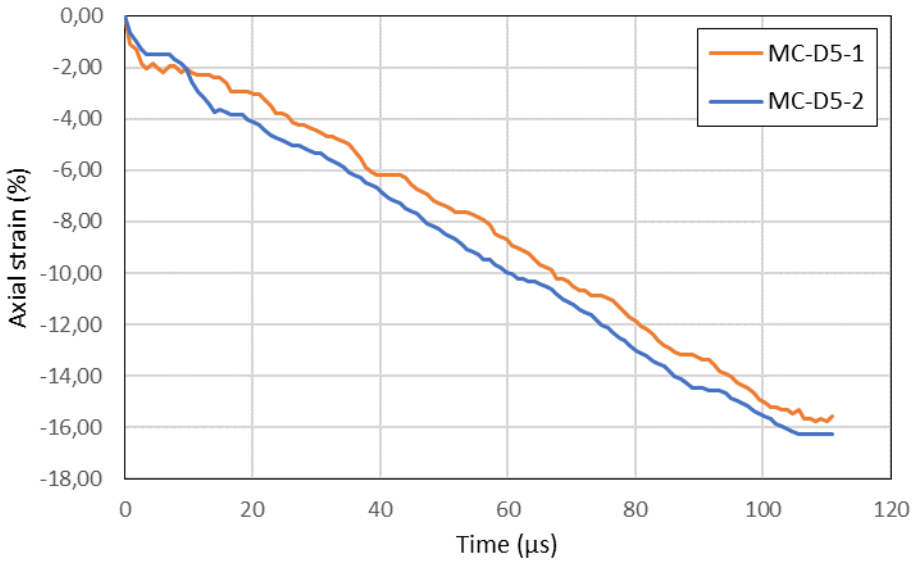

Fig. 8. Axial strain versus time measured from the 128 pictures of ultra-high-speed camera for both QOC tests.

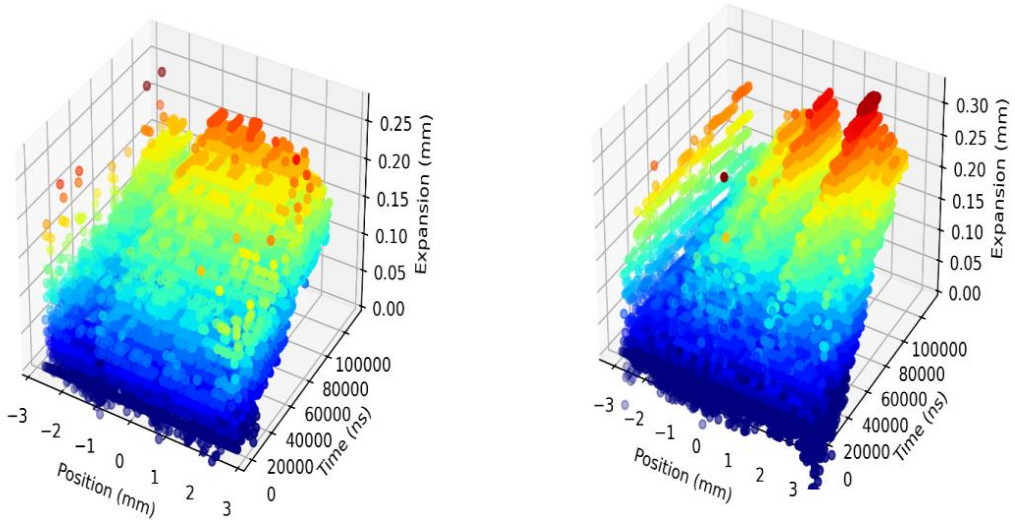

(a) (b)

Fig. 9. Radial expansion as function of time and axial position based on data processing of pictures of ultra-high-speed camera in (a) MC-D5-1 and (b) MC-D5-2 QOC compression tests.

Additional radiographs captured by the ultra-high-speed detector during the MC-D7.5-1 and MC-D7.5-2 QOC compression tests are reported in Annexe 1 (Fig. 10). These radiographs illustrate specific damage modes induced by poor quality of contact at plugs-sample interface (case of MC-D7.5-1 sample) or at cell-sample interface (case of MC-D7.5-1 and MC-D7.5-4 samples). Indeed, in case of MC-D7.5-1 compression test (Fig. 10a), point contact is noted in the first picture (T = 0) and a small is noted between the confining cell and the sample. It may explain early fracturing beneath the contact point (T = 34.32 µs). Next, this crack seems to close itself and second crack network composed of several axial cracks develop. This cracking network stop developing maybe due to limited level of axial strain reached at this end of the loading (about -4%).

In the case of MC-D7.5-4 QOC test (Fig. 10b), the gaps (first picture) at both plugs/sample and cell/sample interfaces disappear in the first 30 µs. Next, deformation process seems to concentrate near the cell/sample interface leading to pore collapse in the vicinity of the contact. In addition, multiple fracturing develops in the sample. At the end of the loading, whereas the axial strain reaches about -8%, small spherical pores look weakly deformed whereas the largest pores, especially those close to the cell-sample interface, seem to be much more fractured and deformed.

In addition, the radial displacement in both (MC-D7.5-1 and MC-D7.5-4) QOC tests was calculated based on data processing of pictures of ultra-high-speed camera by considering the gradient of grey level at sample border. To do so, only the top side was considered as the bottom side was not visible on the pictures. The radial expansion profile as function of time and axial position is reported in Figs 10c (MC-D7.5-1 QOC test) and 10d (MC-D7.5-4 QOC test). First, it should be observed that the high value of radial expansion at position -4 mm visible on the left of both figures (10c and 10d) can be explained by an initial gap at the interface between the sample and the confining cell that is filled in the first microseconds of axial compression. Moreover, in the specific case of sample MC-D7.5-4, a strong increase of radial expansion at a position close to zero (Fig. 10d) is noted. It is the result of the collapse of a large porosity located at sample-cell interface visible on the pictures of ultra-high-speed camera.

These observations seem to indicate a notable influence of pore collapse but also of quality of contact on the deformation and fracture processes taking place at small scale. The observations made by X-ray radiographies appears to be of great interest to assess the role of large pores and the quality of contact at both plugs-sample and cell-sample interfaces.

4. Discussion

The time-resolved correlative macroscopic stress-strain and full-field imaging analysis made in the present work reflects previous, post-mortem, observations made with concrete sample subjected to compression or impact loading. As summarized in [Forquin et al., 2022], cracks initiate from the spherical pores (near the equator) that propagate along the compression axis forming a chimney-shaped (or balcony-shaped) failure pattern, as observed on the fracture surface in a mortar subjected to uniaxial compression loading [Forquin et al., 2007; Arias et al., 2008] (Fig. 11b). Such failure patterns are a result of a low-confinement compression loading. This process was also described in [Forquin, 2003] by simulating the cracking process around a spherical pore within a volume subjected to a uniaxial compression loading (Fig. 11a).

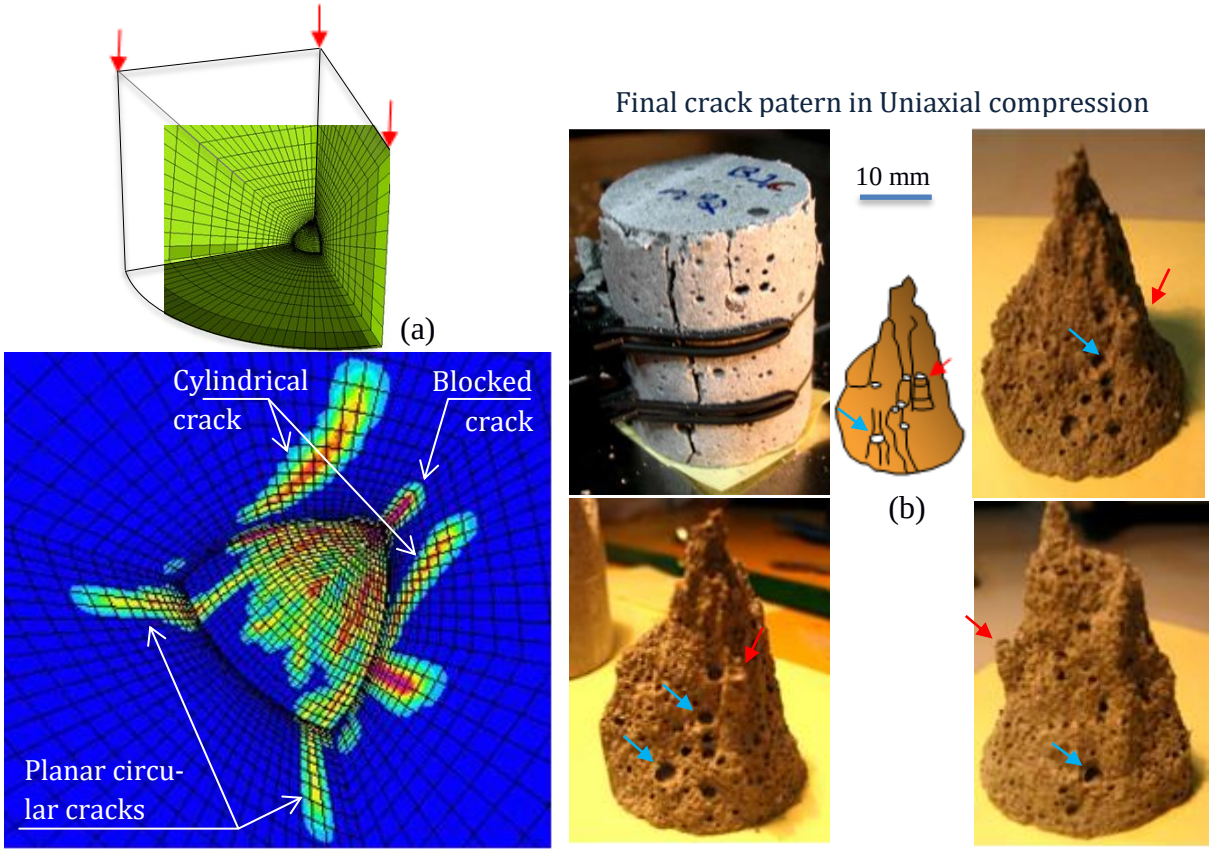

Fig. 11. Damage process induced under uniaxial compression loading. (a) Numerical prediction considering a spherical pore into a cylindrical volume [Forquin, 2003]. (b) Post-test failure pattern of M2 mortar cylindrical sample subjected to a uniaxial compression test [Forquin et al., 2007]. Stress to failure is 67 MPa. Red arrows indicate chimney-shaped fracture surface. Blue arrows indicate balcony-shaped fracture surfaces [Forquin, 2022].

The same kind of mechanism of crack initiation from spherical pore was also observed in a post-mortem analysis of a target subjected to a cylindrical-divergent type of loading. These observations reported in [Forquin, 2003; Forquin and Hild, 2008] were obtained on Ductal® ultra-high-performance concrete (without fibre reinforcement) considering a so-called Edge-On-Impact experiment. In this test, the concrete plate was subjected to the impact of a steel projectile on its edge with a striking velocity about 130 m/s. It led to the following observations: in addition to numerous radial straight cracks crossing through the centre of largest pores, cracks initiated from the equator of spherical pores and propagating along the radial direction (in a cylindrical frame centred in the impact point) were observed leading to cylindrical-shaped fracture surface (Fig. 12). As in the observations made in Fig. 11, it seems to contribute to the start of pore-collapse process in a pore located close to confinement area where much higher compression stresses operate. The time-resolved through volume observations made in the present paper could serve as a first step towards the development of a micro-mechanical model providing a description of micro-crack propagation in concrete under confinement, with enhanced predictive capabilities for describing the relations between pressure, strain-rate and loading path dependant material response.

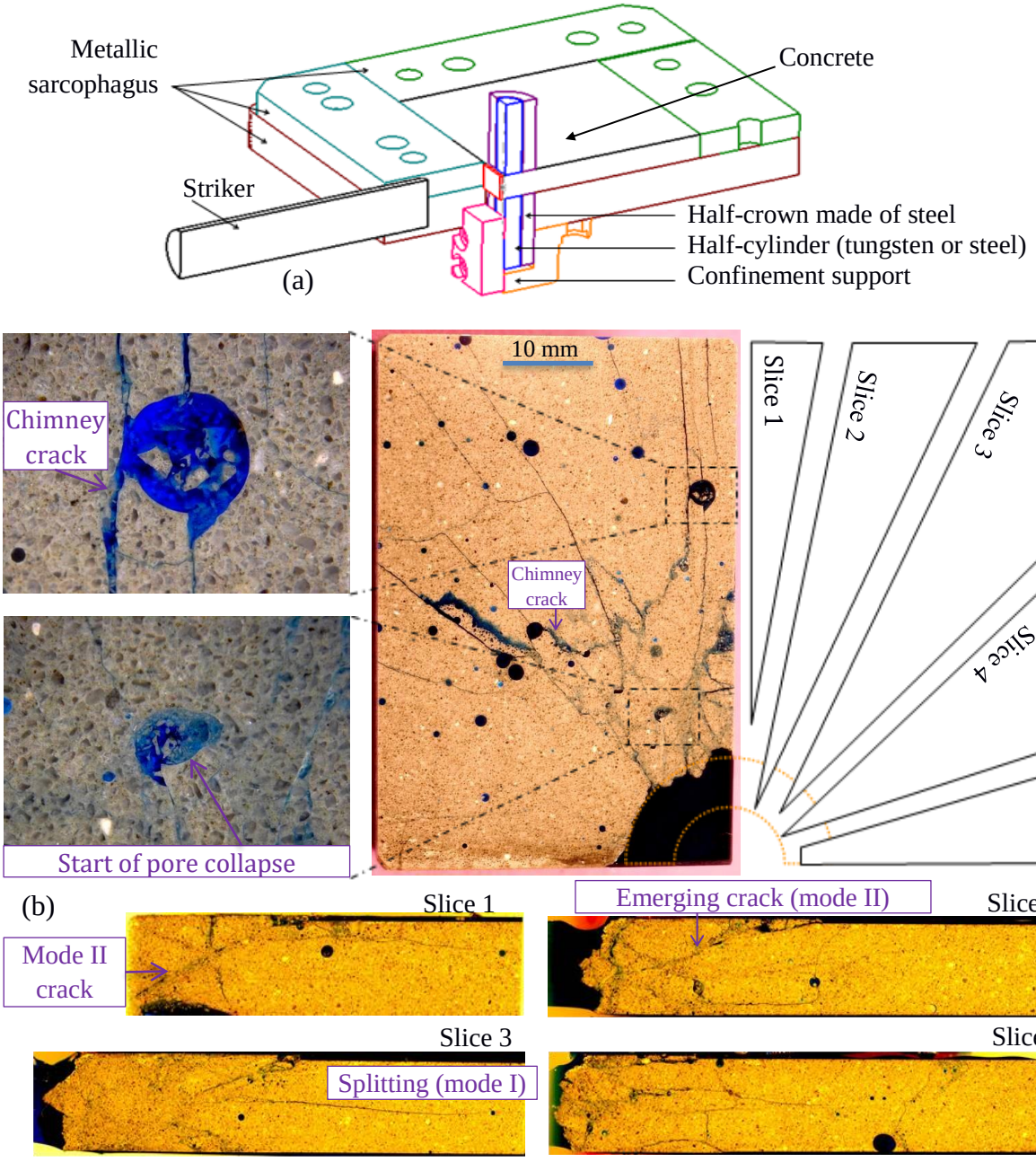

Fig. 12. EOI test conducted with steel projectile and dynamic confinement system applied to Ductal® concrete without fiber. (a) Sarcophagus configuration (b) Sarcophagus configuration, striking velocity: 130 m/s [Forquin, 2022; 2024].

5.CONCLUSION

In the present paper, a testing methodology is proposed to perform time-resolved observations of microcracking mechanisms during high-strain-rate confined loading condition on geomaterials. This configuration consists in performing a Quasi-Oedometric Compression (QOC) experiment in which a cylindrical microconcrete (MC) sample is introduced in polymeric confinement cell and is dynamically compressed along its axial direction by means of SHPB (Split-Hopkinson Pressure Bar). The use of small sample and PC cell allows the visualization of the sample through its thickness with MHz X-ray phase-contrast imaging as available at ID19

beamline of the ESRF. Ultra-high-speed detector assembly, operating at recording frequencies about 1 Mfps (i.e. 880 ns interframe time) in 16 bunch mode was used. By applying a standard Kolsky's processing to data from SHPB data the axial stress and strain temporal profiles were obtained. In addition, data of radial stress and strain within the samples were deduced from a non-linear analysis of the mechanical response of the polycarbonate confining cell instrumented with a strain gauge. The experiments conducted with samples of MC allows the deviatoric and hydrostatic responses of this material to be deduced and time-resolved observation to be made. Finally, the X-ray phase contrast imaging from the captured radiographies provides multiple benefits as it contributes to -assess the quality of contact at both plugs-sample and cell-sample interfaces, -perform time-resolved measurements of axial strain and radial expansion within the sample, -observe the growth of cracks within the sample. In the case a good quality of contact is achieved, a growth of microcrack from the equatorial zone of large spherical pore, which ultimately led to pore collapse was observed. These observations are in-line with previous post-mortem observations made in unconfined compression and in EOI (Edge-On-Impact) experiments. Thanks to the correlative macroscopic mechanical, and microscopic through volume measurements of the microstructural evolution and fracturing, this work contributes to further developments of micromechanics-based numerical modelling strategies accounting for the material dependence and influence of loading path, loading-rate and pressure.

Acknowledgments

The authors acknowledge the European Synchrotron Radiation Facility for provision of synchrotron radiation facilities at imaging beamline ID19 (under the proposal MI-1397, Shock BAG project supported by the European Union's Horizon 2020 research and innovation programme under grant agreement No 870313, Streamline). Bratislav Lukić acknowledges the funding from the EPSRC International Centre to Centre grant with ESRF (EP/W003333/1).

References

Antoniou A., Daudeville L., Marin P., Omar A., Potapov S., 2018. Discrete element modelling of concrete structures under hard impact by ogive-nose steel projectiles. The European Physical J. ST, EDP Sciences, 227(1-2), 143-154

Arias A., Forquin P., Zaera R., Navarro C., 2008. Relationship between bending and compressive behaviour of particle-reinforced cement composites. Composites Part B, 39, 1205-1215.

Burlion, N., Pijaudier-Cabot, G., Dahan, N., 2001. Experimental analysis of compaction of concrete and mortar. Int. J. for Numerical and Analytical Methods in Geomechanics 25, 1467-1486.

Cohen A., Levi-Hevroni D., Fridman P., Chapman D. Rack A. Olbinado M.P., Yosef-Hai A., Eakins D., 2019. In-situ radiography of a split-Hopkinson bar dynamically loaded materials. J. Instrumentation. 14, T06008.

Farbaniec L., Chapman D.J., Patten J.R.W., Smith L.C., Hogan J.D., Rack A., Eakins D.E., 2021. In-situ visualisation of dynamic fracture and fragmentation of an L-type ordinary chondrite by combined synchrotron X-ray radiography and microtomography. ICARUS, 359, 114346.

Forquin P., 2003. Endommagement et fissuration de matériaux fragiles sous impact balistique, rôle de la microstructure. Ph.D. dissertation, Ecole Normale Supérieure de Cachan, France.

Forquin P., Arias A., Zaera R., 2007. An experimental method of measuring the confined compression strength of geomaterials. Int. J. Solids Struct., 44 (13), 4291-4317.

Forquin P., Arias A., Zaera R., 2008a. Role of porosity in controlling the mechanical and impact behaviours of cement-based materials. Int. J. Impact Eng., 35 (3), 133-146.
Forquin P., Gary G., Gatuingt F., 2008b. A testing technique for concrete under confinement at high rates of strain. Int. J. Impact Eng., 35 (6), 425-446.
Forquin P., Arias A., Zaera R., 2008c. Relationship Between Mesostructure, Mechanical Behaviour and Damage of Cement Composites Under High-Pressure Confinement. Exp. Mech., 49, 613–625.
Forquin P., Safa K., Gary G., 2010. Influence of free water on the quasi-static and dynamic strength of concrete in confined compression tests. Cement Concrete Res., 40(2), 321-333.
Forquin P., Hild F., 2008. Dynamic Fragmentation of an Ultra-High Strength Concrete during Edge-On Impact Tests. J. Eng. Mech., 134(4), 302-315.
Forquin P., Sallier L., Pontiroli C., 2015. A numerical study on the influence of free water content on the ballistic performances of plain concrete targets. Mech. Mat. 89, 176-189.
Forquin P., 2017. Brittle materials at high-loading rates: an open area of research. Phil. Trans. R. Soc. A, 375 (2085), 20160436. DOI: 10.1098/rsta.2016.0436.
Forquin P., 2022. Damage in Concrete Subjected to Impact Loading. In: Voyiadjis, G.Z. (eds) Handbook of Damage Mechanics. Springer, Cham, 551–577.
Forquin P., 2024. 4-Dynamic damage and fracture processes in brittle materials. Dynamic Behavior of Materials, Elsevier, 73-116, DOI: 10.1016/B978-0-323-99153-7.00021-9.
Fujikake K., Mori K., Uebayashi K., Ohno T., Mizuno J., 2000. Dynamic properties of concrete materials with high rates of tri-axial compressive loads, Structures under Shock and Impact VI, WIT Press, 511–522.
Gabet T., Malécot Y., Daudeville L., 2008. Triaxial behaviour of concrete under high stresses: Influence of the loading path on compaction and limit states, Cement Concrete Res., 38(3), 403-412.
Hanchak, S.J., Forrestal, M.J., Young, E.R., Ehrgott, J.Q., 1992. Perforation of concrete slabs with 48 and 140MPa unconfined compressive strength. Int. J. Impact Eng. 12(1), 1–7.
Jacobsen Ø., Kristoffersen M., Dey S., Børvik T., 2024. Projectile Impact on Plain and Reinforced Concrete Slabs. J. Dyn. Behavior Mat. 10, 137–159, DOI: 10.107/s40870-023-00379-6.
Kolsky H., 1949. An investigation of mechanical properties of materials at very high rates of loading, Proceedings of the Physical Society London; B 62:676-700.
Li Q.M., Reid S.R., Wen H.M., Telford A.R., 2005. Local impact effects of hard missiles on concrete targets. Int. J. Impact Eng. 32, 224–284.
Lukić B., Saletti D., Forquin P., Blasone M., Cohen A., Rack A., 2024. Single Bunch X-Ray Phase-Contrast Imaging of Dynamic Tensile Failure in Geomaterials. J. Dyn. Behavior Mater. 10(2), 124-136, DOI: 10.1007/s40870-022-00350-x.
Olbinado M.P., Just X., Gelet J.-L., Lhuissier P., Scheel M., Vagovic P., Sato T., Graceffa R., Schulz J., Mancuso A., Morse J., Rack A., 2017. MHz frame rate hard X-ray phase-contrast imaging using synchrotron radiation. Opt. Expr., 25 (12), 13857.
Perkins R.A., Duncan C.J., Johnson D., Stone T.W., Sherburn J.A., Chandler M., Moser R.D., Paliwal B., Prabhu R.K., Hammi Y., 2023. Assessment of a high strength concrete using experimental and numerical methodologies for high strain rate ballistic impacts, Int. J. Impact Eng., 178, 104598, DOI: 10.1016/j.ijimpeng.2023.104598.
Piotrowska E., Forquin P., 2015. Experimental investigation of the confined behavior of dry and wet high-strength concrete: quasi static versus dynamic loading. J. Dyn. Behavior Mat. 1 (2), 191-200.

Piotrowska E., Forquin P., Malecot Y., 2016. Experimental study of static and dynamic behavior of concrete under high confinement: effect of coarse aggregates strength. Mech. Mat., 92, 164–174.

Pournoori, N., Soares, G.C., Lukić, B., Isakov, M., Belone, M.C.L., Hokka, M., Kanerva, M., 2023. In situ damage characterization of CFRP under compression using high-speed optical, infrared and synchrotron X-ray phase-contrast imaging. Compos. - A: Appl. Sci. Manuf., 175, 107766.

Rack, A., Lukić, B., Chapman, D., Strucka, J., Yao, Y., Mughal, K., Efimov, S., Belozerov, O., Krasik, Y., Chittenden, J., Bland, S., Ganzenmuller, G., Cohen, A., Levi-Hevroni, D., Proud, W., Song, P., Eakins, D., 2024. Dynamic loading platforms coupled to ultra-high speed X-ray imaging at beamline ID19 of the European Synchrotron ESRF. High Press. Res.

Sun, X., Sory, D., Liu, K., Lukić, B., Simonian, D., Wong, K.L., Rack, A., Chapman, D., Petrinic, N., Eakins, D., 2024. Effect of temperature on high strain-rate damage evolving in CFRP studied by synchrotron-based MHz X-ray phase contrast imaging. Compos. B Eng., 111445.

Wang, H.C., Liu, K., Lukić, B., Hu, W.R., Braithwaite, C.H., Zhao, J., Rack, A., Zhang, Q.B., 2024. In-situ deformation and fracturing characteristics of geomaterials under dynamic loading: Insights from ultra-high-speed X-ray phase contrast imaging and DEM modelling. Int. J. Rock Mech. Min. Sci., 175, 105656.

Annexe 1

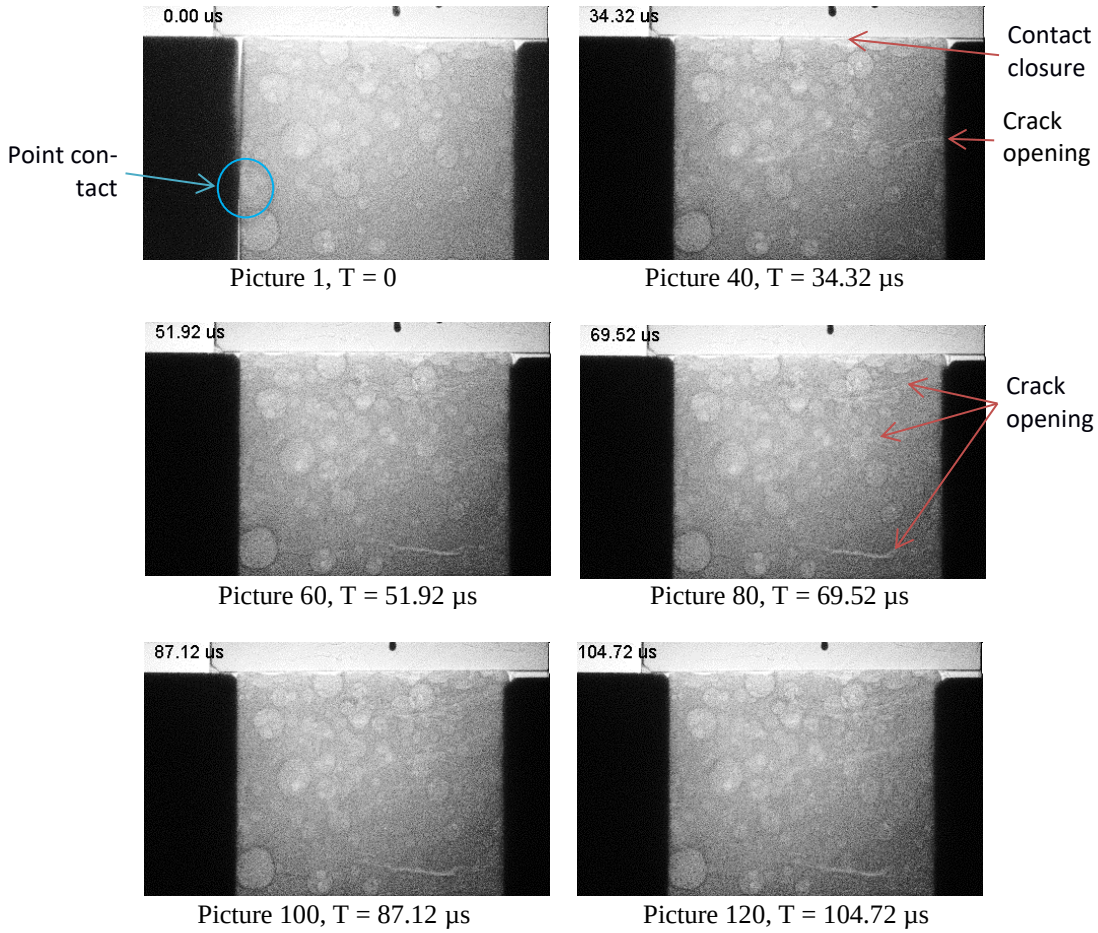

Picture 1, T = 0 | Picture 40, T = 34.32 µs

Picture 60, T = 51.92 µs | Picture 80, T = 69.52 µs

Picture 100, T = 87.12 µs | Picture 120, T = 104.72 µs

(10a) MC-D7.5-1 QOC test

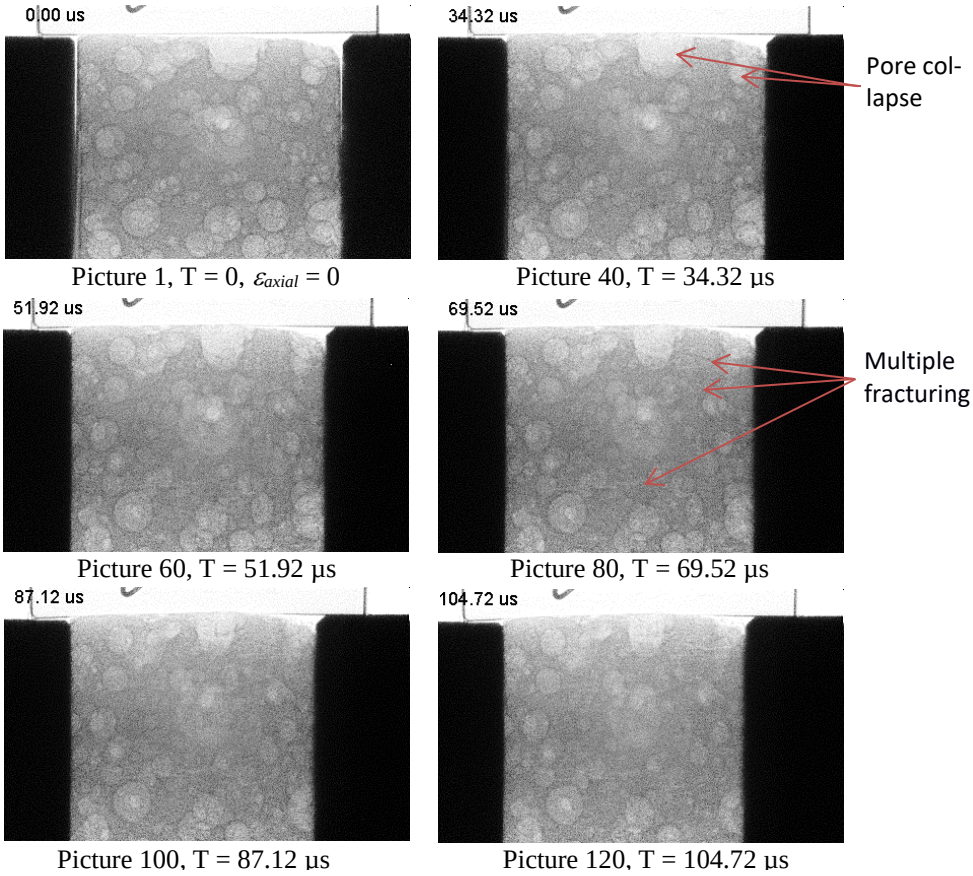

(10b) MC-D7.5-4 QOC test

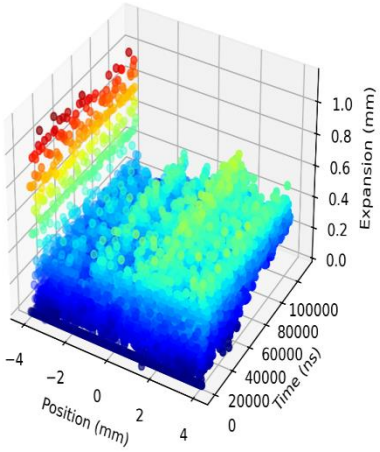

(10c) MC-D7.5-1 QOC test

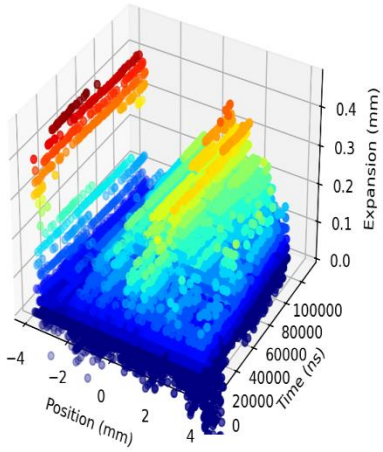

(10d) MC-D7.5-4 QOC test

Fig. 10. Time-resolved observations performed with ultra-high-speed camera in (a) MC-D7.5-1 and (b) MC-D7.5-4 QOC compression tests. Radial expansion as function of time and axial position based on data processing of pictures of ultra-high-speed camera in (c) MC-D7.5-1 and (d) MC-D7.5-4 QOC compression tests.